


Dissolution process of a single bubble under pressure with a large-density-ratio multicomponent multiphase lattice Boltzmann model

Xiaolong He ^{1,2}, Jianmin Zhang ^{1,*}, Qian Yang ^{2,3}, Haonan Peng ¹ and Weilin Xu¹

¹State Key Laboratory of Hydraulics and Mountain River Engineering, Sichuan University, Chengdu 610065, China

²Tianjin Research Institute for Water Transport Engineering, Key Laboratory of Engineering Sediment, Ministry of Transport, Tianjin 300456, China

³Department of Hydraulic Engineering, Tsinghua University, Beijing 100084, China

 (Received 26 August 2020; revised 2 December 2020; accepted 8 December 2020; published 24 December 2020)

A large-density-ratio and tunable-viscosity-ratio multicomponent multiphase pseudopotential lattice Boltzmann model is used to study the dissolution process of a bubble under pressure. The multi-relaxation-time collision operator, exact-difference-method external force scheme, and scaling coefficient k are applied to ensure the numerical stability of the model. The influence of k in the equation of state (EOS) and intermolecule interaction strength on the stationary bubble evolution process are discussed, and the effect of k on thermodynamic consistency is also analyzed. The results indicate that adjusting the scaling coefficient in the EOS changes the surface tension and interface thickness, and that the gas-liquid interface width w is proportional to $1/\sqrt{k}$. Considering the effect of k on the surface tension, interface thickness, and thermodynamic consistency, the scaling coefficient should be between 0.6 and 1. Furthermore, the dissolution process of a single bubble under pressure is studied using the developed model, and it is found that the dissolution mass and concentration of dissolved gas increase linearly with increases in the pressure difference, and that the concentration of dissolved gas is proportional to the gas pressure after the fluid system reaches equilibrium. These results are consistent with Henry's law.

DOI: [10.1103/PhysRevE.102.063306](https://doi.org/10.1103/PhysRevE.102.063306)

I. INTRODUCTION

The growth and dissolution of gas bubbles under different pressure conditions are widespread in natural phenomena and industrial processes, such as carbon dioxide transport in a coal reservoir [1], clinical practice involving human blood and tissue [2], the formation of bubbles in hydraulic systems [3], dissolution and precipitation of supersaturated total dissolved gas in hydraulic engineering [4], and air bubble formation and dissolution in nanoimprint lithography [5]. Gas molecules mainly exist in the form of space-filling gas hydrates after they enter the liquid phase [6,7]. Although bubble sizes range from micrometers to centimeters in the aforementioned phenomena, the mass transfer in the dissolution and growth of gas bubbles originates at the molecular level.

The growth and dissolution process of gas bubbles has received attention from scientists and engineers for a long time. Numerous experimental and numerical studies have investigated bubble growth and dissolution; a subset of the most relevant studies is summarized here [8]. The bubble diameter used to observe the growth and dissolutions process by optical means often ranges from 100 to 300 μm . Krieger *et al.* [9] used a high-resolution optical technique combined with the Epstein-Plesset equation to study the dissolution coefficients of oxygen in different liquids. However, for bubbles of 100–300 μm with larger rise velocities, the gas-liquid interface deformation becomes sharper. Therefore, the gas bubbles

were always fixed by a flat plate or capillary needle tube. Liebermann found that the gas dissolution rate of free bubbles is quite different from that of trapped bubbles [10]. For a fixed bubble near a large impermeable boundary, it is necessary to modify the Epstein-Plesset equation by reducing the bubble diffusivity.

Exhaustive numerical studies on the growth or dissolution of isolated bubbles have been reported over the years, with most macroscopic models falling into one of three categories. The most widespread are Epstein-Plesset solutions based on the quasistationary approximation [6,7,9]. In such models, the ambient process during the entire growth or dissolution process is assumed to remain constant, and a uniform concentration or density field is set as an initial condition. The second method is based on the assumption that the fluid in the gas bubble and the surrounding liquid is the same component [11,12]. The description of the gas-liquid phase change during bubble growth and dissolution is then based on an equation of state (EOS) relating the density, pressure, and temperature of this fluid, and the compressibility of the fluid is also taken into account. The third category is based on the Navier-Stokes equations together with a mass transfer equation to model the mass exchange between the gas and liquid phases [13,14]. This method requires the Rayleigh-Plesset equation to obtain the gas-liquid mass transfer rate. To improve its accuracy, some empirical constants are usually introduced into the Rayleigh-Plesset equation to modify the gas-liquid transition rate. The accuracy of these methods is often limited by their assumptions and the selection of the mass transfer coefficient, making it difficult to simulate the process

*Corresponding author: zhangjianmin@scu.edu.cn

of gas dissolution accurately. While the gas-bubble growth and dissolution process has been analyzed in macroscale approaches, the underlying details of the meso- and microscale processes, which dominate the process behavior in terms of interface evolution, interfacial mass transport, and dissolution concentration distribution, remain unrevealed. Understanding the meso- and microscopic mechanisms during the bubble growth and dissolution process is critical to achieving better predictions of the related multiphase phenomena.

Lattice Boltzmann multiphase models have been extensively developed over the past 30 years. These are diffuse interface models that use a narrow fluid mixture layer instead of a sharp phase interface. They can be divided into four categories: pseudopotential models [15,16], color models [17,18], free-energy models [19,20], and the phase-field model [21]. The pseudopotential models are the most widely used due to their simplicity. This kind of model can be further divided into single-component multiphase flow (SCMP) models and multicomponent multiphase flow (MCMP) models. In pseudopotential models, the gas-liquid interface of the model can be formed automatically through the interaction between fluid particles, thus reducing the computational load of complex interface tracking or capture technology in macroscopic methods [22]. Rapid developments in SCMP models over the past 20 years have eliminated defects such as low density ratios, small kinematic viscosity ratios, thermodynamic inconsistencies, and large spurious currents from the original pseudopotential model. The MCMP pseudopotential model was first proposed by Shan and Doolen [23], and has also experienced rapid developments in the past 10 years. Gradually, the potential for solving mass transfer problems with high density and viscosity ratios has been realized. MCMP pseudopotential models achieve a high density ratio or a high viscosity ratio through one of the following techniques: an appropriate EOS, such as the Peng-Robinson (PR) EOS or Carnahan-Starling (CS) EOS [24–27]; different external force schemes [28,29]; the use of a multi-relaxation-time (MRT) collision operator to improve the numerical stability and density ratio of the model [29,30]; and high-node models such as D2Q24 [31]. MCMP pseudopotential models reflect the distribution of gas component molecules in the liquid component, and have the advantages that no assumptions are made and no empirical formulas are used to describe the mass transfer. Chen *et al.* [26] proposed an MCMP pseudopotential model based on the CS EOS, and simulated the mass transfer and deposition process in a multiphase flow with a gas-liquid density ratio of 152 in pore scale. Stiles and Xue [25] discussed the highest density ratio that could be achieved by an MCMP pseudopotential model with different EOSs, including van der Waals, PR, and CS, and investigated the relationship between interface thickness, maximum virtual velocity, EOS, and the pressure scaling coefficient. The results showed that smaller spurious currents could be obtained by using the CS or PR EOS. Zhu *et al.* [29] combined the MRT collision operator and exact-difference-method (EDM) force scheme with an MCMP pseudopotential model, and simulated the three-phase gas-liquid-solid transformation with a liquid-gas density ratio of ~ 1200 . Chen *et al.* [30] simulated the reactive transport during CO₂ dissolution trapping by combining a high-density-ratio MCMP pseudopotential

model with the MRT collision operator. Deng *et al.* [28] proposed a high-density-ratio MCMP pseudopotential model that satisfies thermodynamic consistency and has an independently adjustable surface tension, and successfully simulated the movement of droplets on the gas diffusion layer surface.

The above-mentioned studies have solved the problems of large density ratios, large viscosity ratios, the adjustment of surface tension, and thermodynamic consistency. However, some key problems related to the rationality of the numerical results given by MCMP pseudopotential models still exist, such as whether the scaling coefficient k of the EOS affects the thermodynamic consistency [25,29,32,33], the validation of thermodynamic consistency, and significant numerical stability issues when the external force terms of SCMP models are extended to MCMP models.

In the present study, we developed an MCMP pseudopotential model with a high density ratio and tunable viscosity ratio. The MRT collision operator, EDM force scheme, and scaling coefficient of EOS are used to ensure numerical stability at large density ratios and various viscosity ratios. This paper discusses the effect of the scaling coefficient of the EOS on surface tension, interface thickness, and thermodynamic consistency, and investigates the influence of the intermolecule interaction strength on the gas component density distribution. Furthermore, the mass transfer process of the gas under different pressure conditions with high liquid-gas density and viscosity ratios is studied using the developed model. The effects of the initial pressure difference and scaling coefficient are discussed, and variations in the gas density field, transport mass, and gas solubility are analyzed.

The remainder of this paper is organized as follows. Section II introduces an MCMP MRT pseudopotential lattice Boltzmann model (LBM) that can be used to simulate multiphase phenomena at high density ratios and various viscosity ratios. Section III verifies the applicability of this model and simulates the mass transfer process of gas under different pressures. Finally, some conclusions are drawn in Sec. IV.

II. MCMP PSEUDOPOTENTIAL MODEL

Compared with the Bhatnagar-Gross-Krook (BGK) collision operator, pseudopotential models with the MRT collision operator [34] have better numerical stability when simulating certain high-density-ratio phenomena [35]. The MRT collision operator, EDM force scheme, and scaling coefficient of the EOS are applied in the present study to improve the density ratio, and are combined with the method proposed by Otomo *et al.* [36] to achieve high viscosity ratios. Particle distribution functions with external force terms in the MCMP pseudopotential model can be written as

$$\begin{aligned} f_{\alpha,i}(\mathbf{x} + \mathbf{e}_i \Delta t, t + \Delta t) \\ = f_{\alpha,i}(x, t) - \sum_j \bar{\Lambda}_{i,j} (f_{\alpha,i} - f_{\alpha,i}^{eq})|_{(x,t)} + S_{\alpha,i}, \quad (1) \end{aligned}$$

where $f_{\alpha,i}$ is the particle distribution function of component α , $f_{\alpha,i}^{eq}$ is the equilibrium distribution, \mathbf{x} is the spatial position, \mathbf{e}_i is the discrete velocity of the i th direction, and Δt is the time step. $\bar{\Lambda} = \mathbf{M}^{-1} \mathbf{A} \mathbf{M}$ is the collision matrix, where \mathbf{M} is the orthogonal transformation matrix, \mathbf{M}^{-1} is the inverse of

\mathbf{M} , and the diagonal matrix $\mathbf{\Lambda}$ is described as [37]

$$\mathbf{\Lambda} = \text{diag}(\tau_p^{-1}, \tau_e^{-1}, \tau_\zeta^{-1}, \tau_j^{-1}, \tau_q^{-1}, \tau_j^{-1}, \tau_q^{-1}, \tau_v^{-1}, \tau_v^{-1}). \quad (2)$$

where the relaxation time τ_v is related to the kinematic viscosity as $\nu = \frac{1}{c_s^2}(\tau_v - 0.5)\Delta t$. The equilibrium distribution function $f_{\alpha,i}^{eq}$ is [26]

$$f_{\alpha,i}^{eq} = \omega_i \rho_\alpha \left[1 + \frac{\mathbf{e}_i \cdot \mathbf{u}_\alpha^{eq}}{c_s^2} + \frac{(\mathbf{e}_i \cdot \mathbf{u}_\alpha^{eq})^2}{2c_s^4} - \frac{\mathbf{u}_\alpha^{eq2}}{2c_s^2} \right], \quad (3)$$

where the weights are $\omega_0 = 4/9$, $\omega_{1-4} = 1/9$, and $\omega_{5-8} = 1/36$; and c_s is the lattice sound speed. The EDM external forces are applied in the present study, and the corresponding equilibrium distribution velocity of component α , \mathbf{u}_α^{eq} , is expressed as [26]

$$\mathbf{u}_\alpha^{eq} = \sum_\alpha \sum_i f_{\alpha,i} \mathbf{e}_i / \sum_\alpha \rho_\alpha, \quad (4)$$

where ρ_α is the density of component α , given by [26]

$$\rho_\alpha = \sum_i f_{\alpha,i}, \quad (5)$$

and $S_{\alpha,i}$ is the external force term of component α . For MRT models, the EDM external force terms [38] can be expressed as

$$S_{\alpha,i} = \mathbf{M}_{i,j}^{-1} [m_{\alpha,j}^{eq}(\rho_\alpha, u_\alpha^{eq} + \Delta u_\alpha) - m_{\alpha,j}^{eq}(\rho_\alpha, u_\alpha^{eq})], \quad (6)$$

where $\Delta u_\alpha = F_{\alpha,\text{total}} \Delta t / \rho_\alpha$, in which $F_{\alpha,\text{total}}$ is the total force acting on the fluid particle of component α . \mathbf{m}^{eq} is the equilibrium distribution moment, and is given by [37]

$$\begin{aligned} \mathbf{m}^{eq} &= \mathbf{M} \mathbf{f}^{eq} = [\rho_\alpha, -2\rho_\alpha + 3(u_{\alpha x}^{eq2} + u_{\alpha y}^{eq2}), \\ &\rho_\alpha - 3(u_{\alpha x}^{eq2} + u_{\alpha y}^{eq2}), u_{\alpha x}^{eq}, \\ &-u_{\alpha x}^{eq}, u_{\alpha y}^{eq}, -u_{\alpha y}^{eq}, u_{\alpha x}^{eq2} + u_{\alpha y}^{eq2}, u_{\alpha x}^{eq} u_{\alpha y}^{eq}]. \end{aligned} \quad (7)$$

The density of the mixed fluid ρ and the actual flow velocity of the fluid \mathbf{u}_p are [26]

$$\rho = \sum_\alpha \rho_\alpha, \quad \mathbf{u}_p = \frac{\sum_\alpha \rho_\alpha \mathbf{u}_\alpha + \frac{\Delta t}{2} \sum_\alpha F_{\alpha,\text{total}}}{\rho}. \quad (8)$$

Pseudopotential models can automatically form the interface through the interaction force from the pseudopotential between particles. For the MCMP pseudopotential model, the interaction force between molecules is divided into two parts: the intramolecule force in the same component and the intramolecule force between different components [29,39]. In the original LBM pseudopotential MCMP model, the same pseudopotential function is applied to calculate the intramolecule force in the same component and the intramolecule force between different components. Once the potential function of each component is determined, the only way to adjust the interaction strength is changing the value of $G_{\alpha,\bar{\alpha}}$, where $G_{\alpha,\bar{\alpha}}$ is the intramolecule strength between two particles [39]. After a lot of $G_{\alpha,\bar{\alpha}}$ values were tried in our early study, which was tedious work, for 0 or positive $G_{\alpha,\bar{\alpha}}$, it takes a longer time to reach equilibrium for Laplace validation. On the other hand, for a negative $G_{\alpha,\bar{\alpha}}$, an attractive force intramolecule force is formed, and the gas components

are mainly distributed in the liquid phase, which is unreasonable. Therefore different intermolecule and intramolecule pseudopotentials are applied in the present study. The intramolecule force is expressed as [26]

$$\mathbf{F}_{\alpha,\alpha} = -G_{\alpha,\alpha} \psi_\alpha(\mathbf{x}) c_s^2 \sum_i w_i \psi_\alpha(\mathbf{x} + \mathbf{e}_i \Delta t) \mathbf{e}_i, \quad (9)$$

where $G_{\alpha,\alpha}$ is the intramolecule interaction strength between two particles and ψ_α is the interparticle potential between particles of the same component. For the D2Q9 LBM, $w_i = 1/3$ when $|\mathbf{e}_i| = 1$ and $1/12$ when $|\mathbf{e}_i| = 2$ [40]. ψ_α can be calculated after a nonideal gas EOS is introduced as [41]

$$\psi_\alpha(\rho_\alpha) = \sqrt{\frac{2(p_\alpha - \rho_\alpha c_s^2)}{G_{\alpha,\alpha} c_s^2}}, \quad (10)$$

and the intermolecule force can be expressed as [26]

$$\mathbf{F}_{\alpha,\bar{\alpha}} = -G_{\alpha,\bar{\alpha}} \varphi_\alpha(\mathbf{x}) c_s^2 \sum_i w_i \varphi_\alpha(\mathbf{x} + \mathbf{e}_i \Delta t) \mathbf{e}_i, \quad (11)$$

where $G_{\alpha,\bar{\alpha}}$ is the intermolecule strength between two particles, and φ_α is the interparticle potential between different components [39], expressed as

$$\varphi_\alpha = a_\alpha - \exp(-\rho_\alpha / \rho_{\alpha 0}), \quad (12)$$

where the parameters a_α and $\rho_{\alpha 0}$ depend on the simulation conditions. The CS EOS [41] is used in the present study:

$$p_\alpha = \rho_\alpha R_g T \frac{1 + b\rho_\alpha/4 + (b\rho_\alpha/4)^2 - (b\rho_\alpha/4)^3}{(1 - b\rho_\alpha/4)^3} - a\rho_\alpha^2, \quad (13)$$

where $a = 0.4963 R_g^2 T_c^2 / p_c$ and $b = 0.1873 R_g T_c / p_c$ are parameters, T_c is the critical temperature, and p_c is the critical pressure. Kupershtokh [32] introduced the scaling coefficient k to the EOS to increase the liquid-gas density ratio of pseudopotential models:

$$p'_\alpha = k p_\alpha = k \left[\rho_\alpha R_g T \frac{1 + b\rho_\alpha/4 + (b\rho_\alpha/4)^2 - (b\rho_\alpha/4)^3}{(1 - b\rho_\alpha/4)^3} - a\rho_\alpha^2 \right]. \quad (14)$$

The total pressure of the fluid system is [26]

$$p_{\text{total}} = c_s^2 \sum_\alpha \rho_\alpha + \frac{1}{2} c_s^2 \sum_\alpha G_{\alpha,\alpha} \psi_\alpha^2 + \frac{1}{2} c_s^2 \sum_\alpha G_{\alpha,\bar{\alpha}} \varphi_\alpha \varphi_{\bar{\alpha}}. \quad (15)$$

In the present study, the method proposed by Otomo *et al.* [36] is adopted to achieve high viscosity ratios, and the relaxation coefficient τ_v in (2) can be expressed as the relaxation coefficient of mixed fluids:

$$\tau_v = \left(\frac{\nu_{\text{mix}}}{c_s^2} \right) + 0.5, \quad (16)$$

where ν_{mix} is the viscosity of the mixed fluid, given by

$$\nu_{\text{mix}} = \kappa \nu_\alpha + (1 - \kappa) \nu_{\bar{\alpha}}, \quad (17)$$

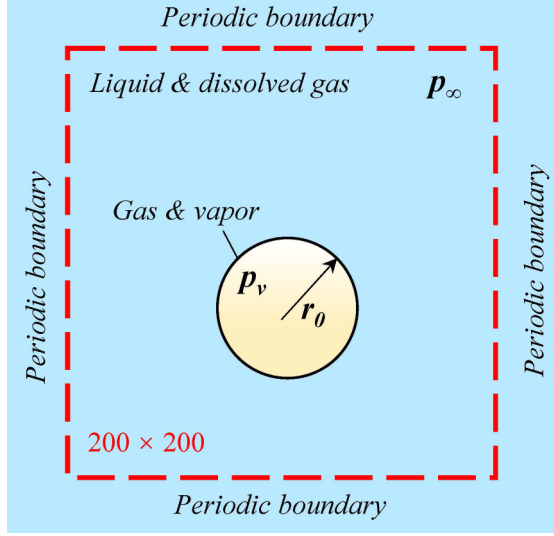


FIG. 1. Schematic diagram for Laplace's law and bubble dissolution, where the rectangular area with dashed box is the computational domain.

in which κ is a smoothing function that can be simply taken as

$$\kappa = \rho_\alpha / \sum_\alpha \rho_\alpha, \quad (18)$$

and $\nu_\alpha = \frac{1}{c_\alpha^2}(\tau_{v\alpha} - 0.5)\Delta t$ is the viscosity of component α , which is related to the relaxation coefficient $\tau_{v\alpha}$ of α .

III. SIMULATION RESULTS AND DISCUSSION

A. Physical problems

Gas dissolved under pressure exists in many natural phenomena and engineering applications, such as bubble disease in fish and total dissolved gas in hydraulic engineering. In this section, two typical two-phase gas-liquid flow phenomena, namely, Laplace's law and a single bubble dissolved under pressure, are used as validation examples to check the applicability of the model developed in the previous section. The effect of the pressure difference between water and the surrounding fluid, the influence of the scaling coefficient of the EOS on the bubble dissolution process, and the associated dynamic behavior are analyzed in detail. A schematic diagram of the computational domain is present in Fig. 1. When the bubble is small enough (less than $50 \mu\text{m}$), it will be influenced by buoyancy and drag forces, leading to a very small rise in velocity. Thus, the influence of buoyancy and drag forces is not considered in the present study. A bubble of radius $R_0 = 50 \text{ lu}$ (where "lu" denotes lattice units) is placed in the center of the $200 \text{ lu} \times 200 \text{ lu}$ computational domain. p_∞ is the pressure of the surrounding liquid and p_v is the pressure in the bubble. The pressure difference between the bubble and the surrounding liquid is obtained by adjusting the liquid phase density of the liquid component.

B. Laplace's law

The MCMP pseudopotential model for large density and viscosity ratios is firstly validated with respect to Laplace's law. After the bubble reaches the equilibrium state, the surface tension σ is proportional to the pressure difference inside and outside of the bubble, and is expressed as

$$\Delta p = \frac{\sigma}{R}. \quad (19)$$

Two-component two-phase flow is simulated in this study. The liquid component is treated as a nonideal fluid while the gas component is treated as an ideal gas. The liquid component is denoted by the subscript 1, and the gas component is denoted by the subscript 2; the intramolecule interaction strengths are set as $G_{11} = -1.0$ and $G_{22} = 0$, respectively. The intermolecule interaction strengths are set as $G_{12} = G_{21} = 0.0005$. The intermolecule pseudopotential, first proposed by Yu [39], is introduced in the present study:

$$\varphi_1(\rho_2) = 1 - \exp(-\rho_2/\rho_{20}), \quad (20)$$

$$\varphi_2(\rho_1) = a_0 - \exp(-\rho_1/\rho_{10}), \quad (21)$$

where a_0 , ρ_{10} , ρ_{20} are constant parameters; $0 < a_0 < -1$. These parameters are critical for numerical stability, although determining their values is tedious work. Yu [39] indicated that they mainly depend on the simulation conditions, such as the dimensionless temperature T/T_c . In the present study, the parameters are set to $a_0 = 0.005$, $\rho_{10} = -\frac{0.0008}{\log(a_0)}$, and $\rho_{20} = 0.0003$. In the CS EOS, the parameters in (13) are set to $a = 1$, $b = 4$, $R_g = 1$, and the corresponding temperature is $T = 0.58T_c$. The corresponding density field is initialized as

$$\rho(x, y) = \frac{(\rho_{\alpha\text{-out}} + \rho_{\alpha\text{-in}})}{2} + \frac{(\rho_{\alpha\text{-out}} - \rho_{\alpha\text{-in}})}{2} \times \tanh \left[\frac{2(\sqrt{(x-x_0)^2 + (y-y_0)^2} - R_0)}{w} \right]. \quad (22)$$

The initial density of component 1 in the bubble is $\rho_{l\text{-in}} = 0.0001$ and the initial density of component 2 in the bubble is $\rho_{g\text{-in}} = 0.0003$, while the initial density of component 1 outside the bubble is $\rho_{l\text{-out}} = 0.42$ and the initial density of component 2 outside the bubble is $\rho_{g\text{-out}} = 0.000001$. The initial corresponding liquid-gas density ratio is $(\rho_{g\text{-out}} + \rho_{l\text{-out}})/(\rho_{g\text{-in}} + \rho_{l\text{-in}}) = 1050$. The initial interface thickness w is set to 5 lu [35], and (x_0, y_0) is the center of the bubble. The relaxation coefficients in the diagonal matrix Λ are taken as $\tau_\rho^{-1} = \tau_j^{-1} = 1.0$, $\tau_e^{-1} = \tau_\zeta^{-1} = 1.1$, and $\tau_q^{-1} = 8(2 - \tau_v)/(8 - \tau_v)$ [26].

A series of bubbles with initial radii of $R_0 = 40, 45, 50, 55, 60$ are selected to calculate the surface tension on the interface, and different EOS scaling coefficients $k = 0.05, 0.1, 0.3, 0.6, 1.0$ are chosen. The intermolecule interaction strength is set as $G_{12} = G_{21} = 0.0005$. The relaxation coefficient of the component 2, τ_v , is chosen as $\tau_g = 1.0625$, while the relaxation coefficient of the component 1, τ_v , is chosen as $\tau_l = 0.5375$ with a corresponding viscosity ratio of $\nu_g/\nu_l = 15$. Figures 2(a)–2(c) show the component 2 density distribution, component 1

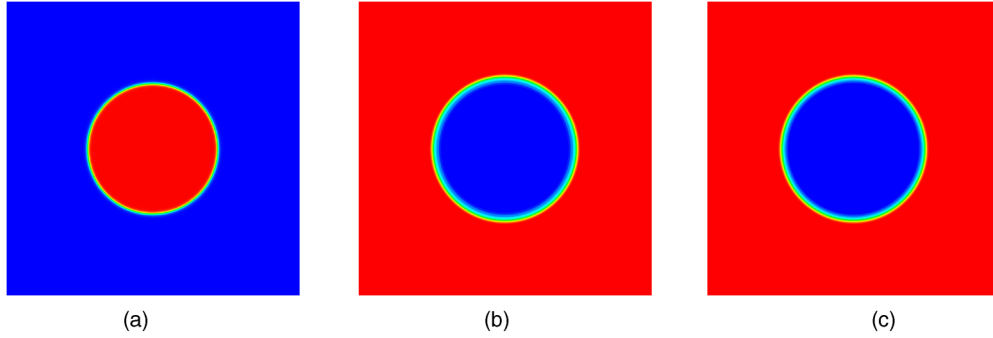


FIG. 2. Density distribution after bubble reaches equilibrium ($k = 0.6$, $R_0 = 50$): (a) component 1 density distribution, (b) component 2 density distribution, and (c) total density distribution.

density distribution, and total density distribution after the bubble reaches equilibrium with $k = 0.6$, $R_0 = 50$, respectively. The results indicate that the interface thickness of component 1 is slightly thinner than that of component 2 and the total density field.

Laplace’s law states that $\Delta p = \sigma/R$; that is, the surface tension σ is proportional to the pressure difference, where Δp is the pressure difference between the interior and exterior of the bubble and R is the radius of the bubble when it reaches equilibrium. The relationship between the pressure difference inside and outside the bubble and the drop radii for five different k values are shown in Fig. 3. The numerical results agree well with the theoretical analysis, with a linear relationship between Δp and $1/R$. The results also show that the surface tension increases as k increases. These results mean that the surface tension can be adjusted slightly through the EOS scaling coefficient.

Comparing the maximum density ratio and the maximum viscosity ratio in the present study with those from previous studies (see Table I), our modified MCMP pseudopotential model with the MRT collision operator can achieve both high density ratios and high viscosity ratios, with a maximum density ratio of 1050 and a viscous coefficient ratio of 15.

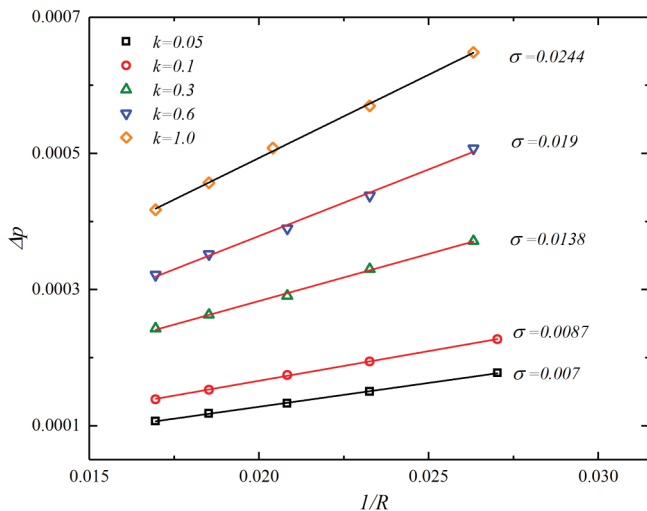


FIG. 3. Relationship between pressure difference inside and outside the bubble and drop radii for five different k values.

The value of $G_{\alpha,\alpha}$ ranges from -0.5 to -40 to analyze its effect on density and spurious currents distribution, and the results are presented in Fig. 4. Both Li *et al.* [35] and Yuan and Schaefer [41] indicated that the $G_{\alpha,\alpha}$ will be canceled when calculating the macrovariables such as ρ , p , and \mathbf{u} . The only requirement for $G_{\alpha,\alpha}$ is to ensure that the whole term inside the square root is positive. As shown in Fig. 4(a), the distribution of the density of component 1 and component 2 does not change with $G_{\alpha,\alpha}$ decreasing from -0.5 to -40 , and the flow field distribution is not influenced by $G_{\alpha,\alpha}$ as shown in Fig. 4(b).

Another interesting thing is that changing the value of $G_{\alpha,\bar{\alpha}}$ leads to the variation of density distribution of component 1 as shown in Fig. 5, making the model thermodynamic inconsistent. A series of $G_{\alpha,\bar{\alpha}}$ is applied here, with $G_{\alpha,\bar{\alpha}}$ value ranges from 0.0007 to 0.0001. When $G_{\alpha,\bar{\alpha}} \geq 0.0006$ or $G_{\alpha,\bar{\alpha}} \leq 0.0001$, the simulation is not convergent, and with $G_{\alpha,\bar{\alpha}} = 0.0005$, the best thermodynamics consistency is obtained for a large density ratio. When $G_{\alpha,\bar{\alpha}}$ decreases from 0.0005 to 0.0001, the maximum spurious current decreases, but the interface thickness stays stable.

C. Thermodynamic consistency

Previous research indicates that the scale coefficient k is an effective parameter for obtaining numerically stable simulations with large density ratios [25,29,33]. Hu *et al.* [33] introduced the scale coefficient k into an SCMP pseudopotential model, and declared that k did not influence the thermodynamic consistency. Later, Stiles and Xue [25] introduced k into an MCMP model with the BGK collision operator, and found that the gas density decreases with any decrease in k at large density ratios, which does not satisfy the requirements for thermodynamic consistency. Recently, Zhu *et al.* [29] introduced k into an MCMP pseudopotential model with the MRT collision operator, and found that the total liquid-gas density ratio fluctuates in a small range. The aforementioned studies have shown that, for different models, the influence of k varies, especially for large density ratios. Thus, it is necessary to discuss the influence of k in the present study. In this subsection, the influence of the scale coefficient k on the interface thickness, spurious currents, and density distribution is investigated.

The density profiles of component 1 and component 2 at $y = 100$ lu with $k = 0.1, 0.5, 1$ are shown in Fig. 6.

TABLE I. Maximum density ratio and viscosity ratio of present study and previous studies.

	Maximum density ratio	Maximum viscosity ratio	Thermodynamic consistency analysis	Scale coefficient k	Collision operator
Bao and Schaefer [24]	10000	1	No	No	BGK
Chen <i>et al.</i> [26]	152	1	No	No	BGK
Stiles and Xue [25]	500	1	Yes	Yes	BGK
Zhang <i>et al.</i> [27]	10.42	1	No	No	BGK
Zhu <i>et al.</i> [29]	1273	1	No	Yes	MRT
Deng <i>et al.</i> [28]	835	16.152	Yes	No	BGK
Present study	1050	15	Yes	Yes	MRT

Considering its effect on thermodynamic consistency, we focus on the density distribution of component 1 in the bubble. The density of component 1 in the bubble decreases from 1.06×10^{-4} to 7.5×10^{-5} as k increases from 0.1 to 1.0, with the total density ratio ranging from 750 to 890. Different values of k exert a significant influence on the density distribution of both components, but have little effect on the density distribution of component 1 in the surrounding liquid.

Figure 7 compares the numerical output with the analytical results under different k values. The results show that a high density ratio can be obtained under different scaling factors with the EDM force scheme. The liquid density

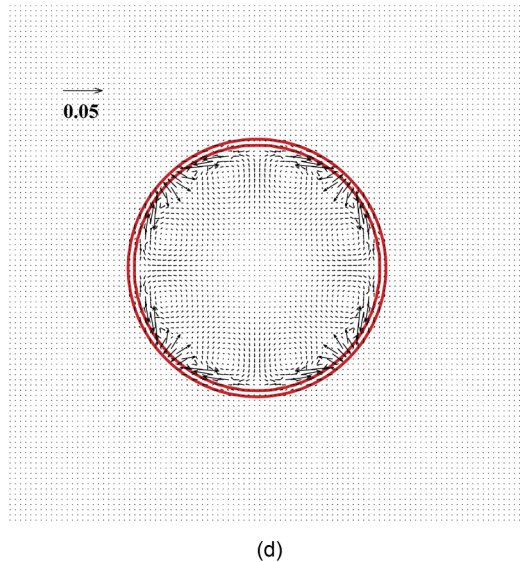
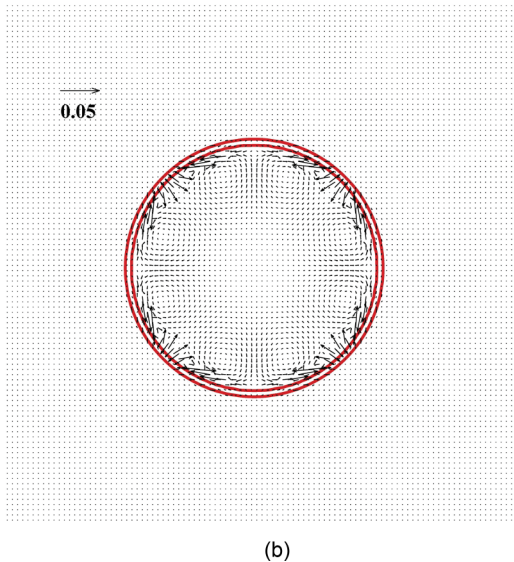
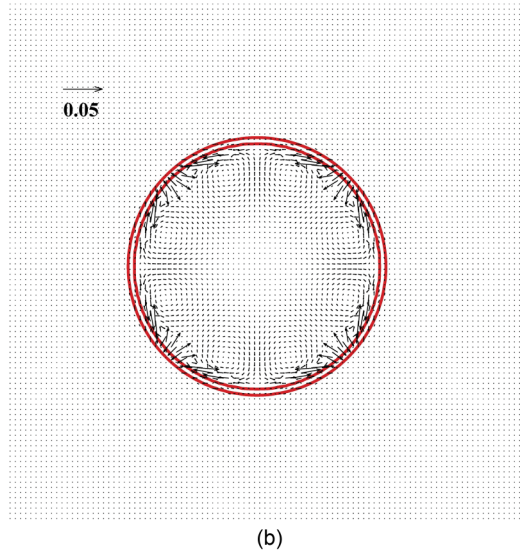
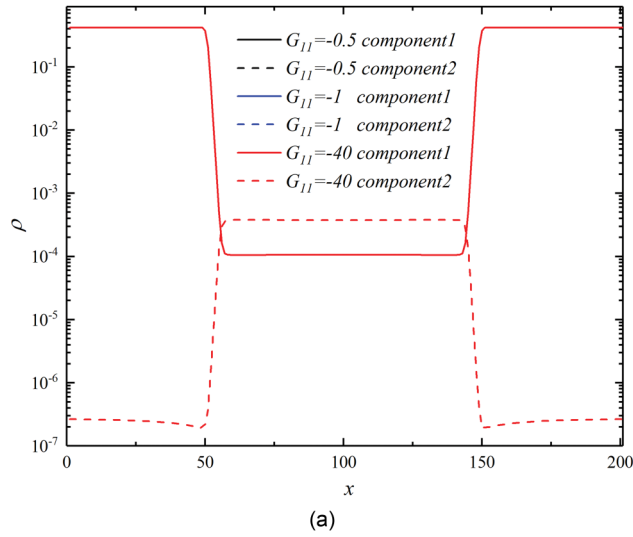


FIG. 4. The distribution of (a) density field of component 1 and component 2 with the different intermolecule interaction strength $G_{\alpha,\alpha}$ at $y = 100$ lu. The velocity distribution in the computation domain with (b) $G_{\alpha,\alpha} = -0.5$, (c) $G_{\alpha,\alpha} = -1$, and (d) $G_{\alpha,\alpha} = -40$.

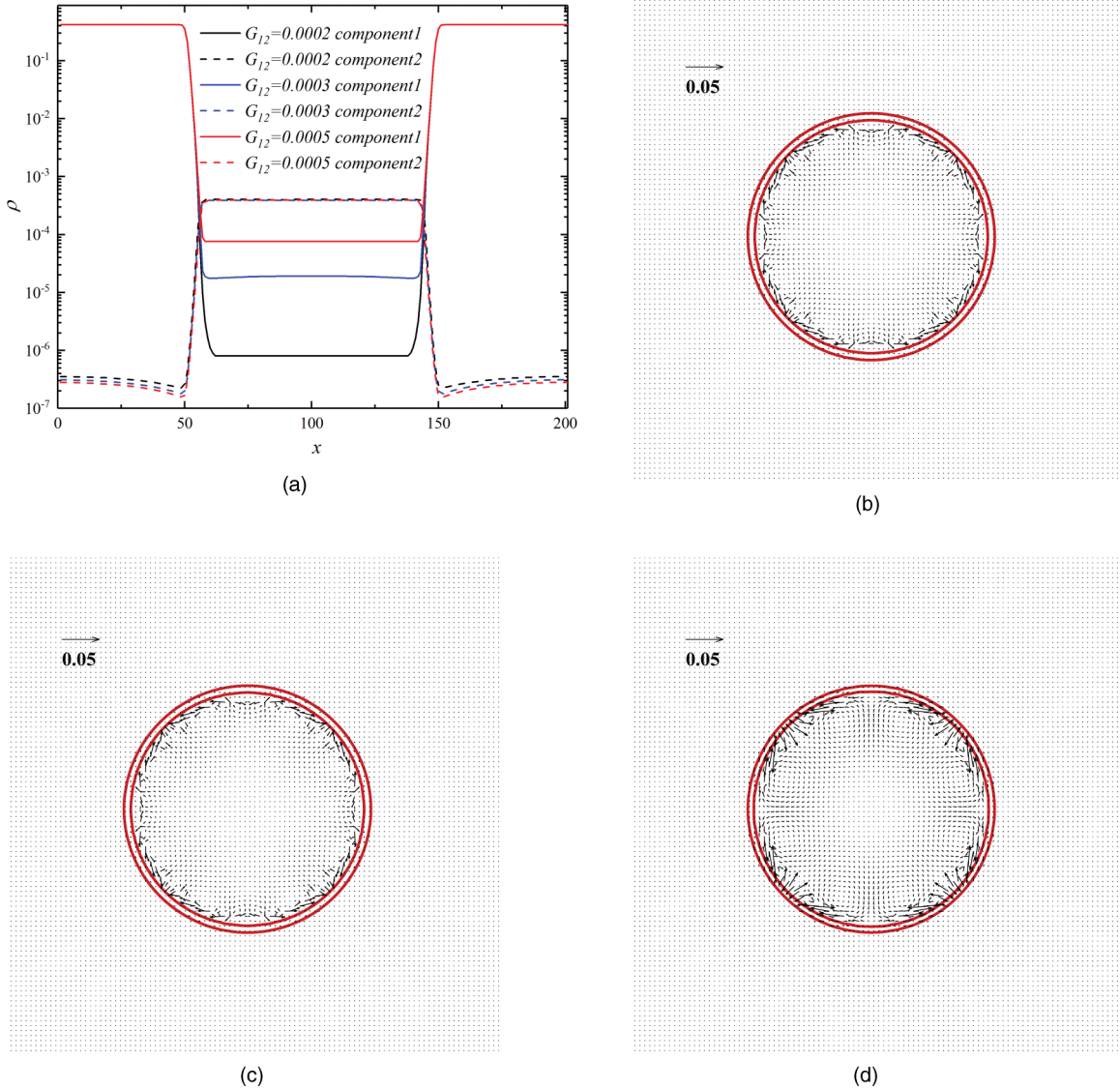


FIG. 5. The distribution of (a) density field of component 1 and component 2 with the different intermolecule interaction strength $G_{\alpha, \bar{\alpha}}$ at $y = 100$ lu. The velocity distribution in the computation domain with (b) $G_{\alpha, \bar{\alpha}} = 0.0002$, (c) $G_{\alpha, \bar{\alpha}} = 0.0003$, and (d) $G_{\alpha, \bar{\alpha}} = 0.0005$.

of component 1 agrees well with the analytical result for different scale coefficients. However, the gas phase density in component 1 deviates from the theoretical results when $T/T_c \leq 0.65$, and the deviation increases as T/T_c decreases. It is also apparent that, for $T/T_c \geq 0.65$, the influence of k on the thermodynamic curve is small. The value of k gradually exerts a greater influence when $T/T_c \leq 0.6$, which is consistent with the research of Hu *et al.* [33]. The model with the EDM external force scheme used in the present study does not achieve thermodynamic consistency when $T/T_c \leq 0.65$. However, the effect of temperature changes is not considered in the simulations of the bubble dissolution process, and so the above-mentioned EDM will be used in later discussions. A corresponding model with good thermodynamic consistency [28] will be extended to the MRT mode in a future study.

The distribution of pressure along the x direction at $y = 100$ lu with $k = 0.1, 0.5$, and 1 is shown in Fig. 8. The decrease of the k value has little effect on the gas phase pressure, but the liquid pressure decreases dramatically, due

to the EOS parameters of component 1 being changed by modifying the scaler k . An unphysical phenomenon of sharp pressure fluctuation with negative pressure exists at the interface points, which results from the large density gradient near the interface, and also exists in earlier studies of large single-component [22,33] and multicomponent [25,26] pseudopotential models.

D. Effect of scale coefficient k

Stiles and Xue [25] suggested that the scaling coefficient k exerts a significant influence on the distribution range and magnitude of spurious currents and the thickness of the interface. Therefore, the influence of k in the present model is now discussed. Figure 9 shows the magnitude and distribution of spurious currents when $R = 50$ lu with different k values while the fluid system reaches the equilibrium state. In Fig. 9, the inner contour line is $\rho = 0.1(\rho_{g-out} + \rho_{l-out} + \rho_{g-in} + \rho_{g-out})$ and the outer contour

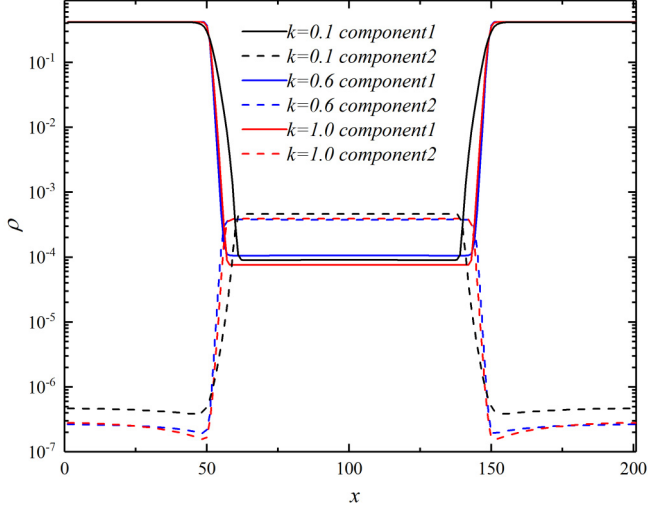


FIG. 6. Density profile after bubble reaches equilibrium of different components at $y = 100$ lu with different k values.

line is $\rho = 0.9(\rho_{g-out} + \rho_{l-out} + \rho_{g-in} + \rho_{g-out})$, and the vertical distance between the two is defined as the interface thickness. As k increases, the range of spurious currents becomes larger, the maximum spurious currents move closer to the interface, and the interface thickness decreases. The results show that the spurious currents mainly stay in the gas phase due to the low inertia of the gas phase. Figure 10 shows the maximum spurious current, interface thickness, and surface tension changes with respect to k for an initial bubble radius of $R_0 = 50$ lu. The results show that the surface tension decreases with k . As k decreases from 1 to 0.05, the surface tension decreases by 70%, from 0.0244 to 0.007. The maximum spurious current also decreases with k : as k decreases from 1 to 0.05, the maximum spurious current decreases to just $0.0056 \text{ lu tu}^{-1}$, which is 18% of the maximum spurious current when $k = 1.0$. Furthermore, the interface thickness

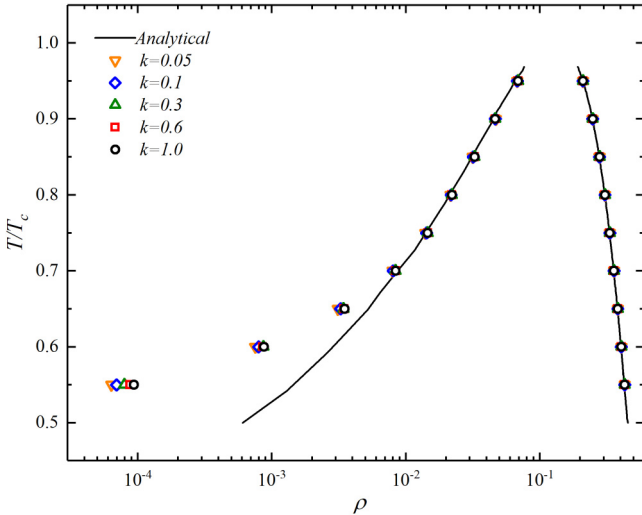


FIG. 7. Comparison of thermodynamic curves in theoretical solution with the EDM force scheme combined with different scale coefficient k values.

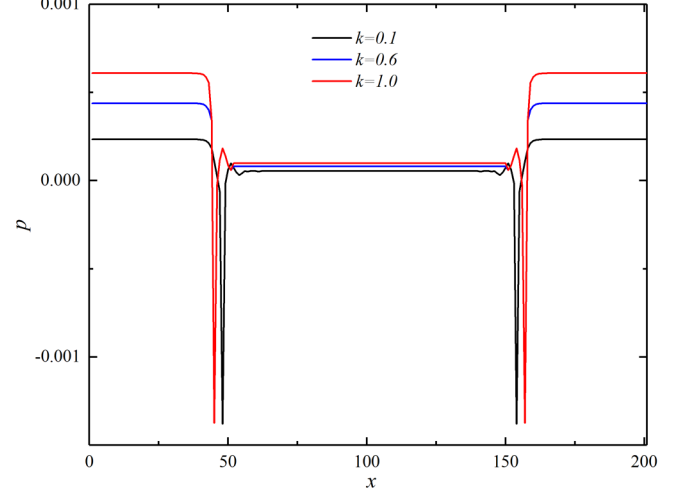


FIG. 8. Pressure distribution after bubble reaches equilibrium at $y = 100$ lu with different k values.

w increases as k decreases. In the present study, when the interface thickness w is 14 lu with $k = 0.05$, this is nearly 30% of the bubble radius, which is unphysical. However, the interface thickness decreases to 5 lu with k increases to 0.6, and the corresponding maximum spurious current is $0.0146 \text{ lu tu}^{-1}$ in present study, which is much smaller than the maximum spurious current reported by Bao and Schaefer [24] with 0.033 lu tu^{-1} (density ratio 971) and that observed by Chen *et al.* [26] with 0.05 (density ratio 152).

Greater interface thickness reduces the density gradient and increases the numerical stability, but it affects the bubble deformation and the mass exchange rate [42,43]. Li *et al.* [35] pointed out that the numerical stability of LBM increases as the interface thickness w increases. However, the numerical simulation results become unphysical if the interface thickness is too large, so it was suggested that the interface thickness should be 4–5 lu. Li *et al.* [35] pointed out the interface thickness is proportional to $1/\sqrt{a}$ when the parameter a is undetermined. The scaling coefficient k is used in the EOS, which means new parameters are applied in CS EOS as

$$p'_\alpha = \rho_\alpha R'_g T \frac{1 + b\rho_\alpha/4 + (b\rho_\alpha/4)^2 - (b\rho_\alpha/4)^3}{(1 - b\rho_\alpha/4)^3} - a' \rho_\alpha^2, \quad (23)$$

where $R'_g = kR_g$, and $a' = ka$. The interface thickness is proportional to $1/\sqrt{a'}$, which also can be presented as $w \propto 1/\sqrt{ka}$. However, the parameter a is undetermined in the study of Li *et al.* [35]. Once a has been determined, the interface thickness w is only proportional to $1/\sqrt{k}$. The simulation results show that the thickness of the interface w is proportional to $1/\sqrt{k}$ with $a = 1$ and $R_0 = 50$ lu, as shown in Fig. 11. To ensure that the interface thickness satisfies both numerical stability and physical phenomena, it is suggested that k should be set in the range 0.6–1.

The chemical potential is the driving force for isothermal mass transport, and is partial molar Gibbs free energy at constant pressure [44]. The chemical potential can be derived

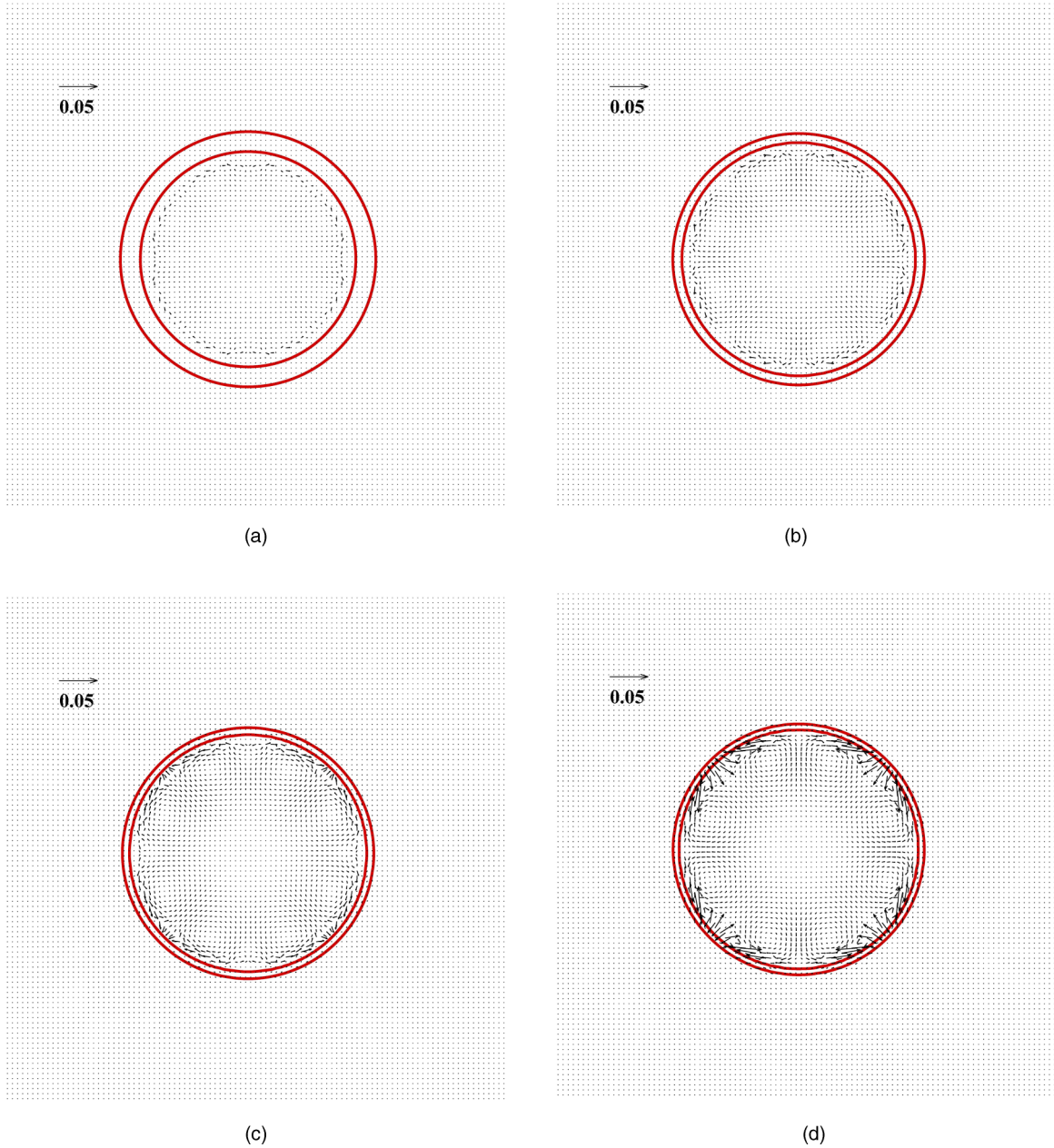


FIG. 9. Distribution of spurious currents with $R_0 = 50$ with different values of k : (a) $k = 0.05$, (b) $k = 0.3$, (c) $k = 0.6$, and (d) $k = 1$.

from the free energy functional [43,44,45]:

$$\mu = \phi'(\rho) + \sigma \nabla^2 \rho \tag{24}$$

where μ is the chemical potential, ϕ is the bulk free energy density at a given temperature, and σ is the surface tension. For CS EOS, the chemical potential is [45]

$$\mu = R_g T \left[\frac{3 - b\rho/4}{(1 - b\rho/4)^3} + \ln \rho + 1 \right] - 2a\rho - \sigma \nabla^2 \rho. \tag{25}$$

The chemical potential distribution along the x direction at $y = 100$ lu with $k = 0.1, 0.5$, and 1 is shown in Fig. 12. Due to the density distribution of components 1 and 2 varying very little as shown in Fig. 6, the chemical potentials almost overlap with each other except on the gas-liquid interface. A dramatic pressure fluctuation exists on the gas-liquid interface which results from the large density gradient, the fluctuation

range, and amplitude of chemical potential increases as the value of scalar coefficient k decreases.

Following the study of Benzi *et al.* [46], the surface tension σ is defined as

$$\sigma = \int_{-\infty}^{+\infty} (p_{yy} - p_{xx}) dy, \tag{26}$$

where p_{yy} and p_{xx} are the normal and transverse components of the pressure tensor. Through theoretical analysis, the surface tension caused by pressure from the intermolecule force is composed of two terms, including $-\frac{1}{2}G_{11}c_s^4|\partial_y\psi_1|^2$ from component 1 and $-\frac{1}{2}G_{22}c_s^4|\partial_y\psi_2|^2$ from component 2. The surface tension caused by pressure from the intramolecule force is also composed of two terms, including $-\frac{1}{2}G_{12}c_s^4|\partial_y\varphi_1|^2$ from component 1 and $-\frac{1}{2}G_{21}c_s^4|\partial_y\varphi_2|^2$ from

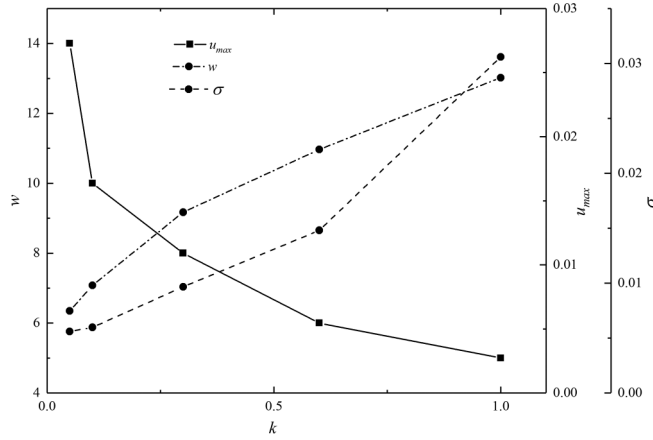


FIG. 10. Relationship between interface thickness or surface tension and scaling coefficient k of EOS .

component 2. The surface tension can be expressed as

$$\sigma = -\frac{1}{2}c_s^4 \int_{-\infty}^{+\infty} (G_{11}|\partial_y\psi_1|^2 + G_{22}|\partial_y\psi_2|^2 + G_{12}|\partial_y\varphi_1|^2 + G_{21}|\partial_y\varphi_2|^2)dy. \quad (27)$$

In the present study, G_{22} is set as 0, leading to the surface tension caused by pressure from the intermolecule force being

$$\sigma_{\text{inter}} = -\frac{1}{2}G_{11}c_s^4 \int_{-\infty}^{+\infty} (|\partial_y\psi_1|^2)dy. \quad (28)$$

The G_{12} has the same value of G_{21} , leading to the surface tension caused by pressure from the intramolecule force being

$$\sigma_{\text{intra}} = -\frac{1}{2}G_{21}c_s^4 \int_{-\infty}^{+\infty} (|\partial_y\psi_1|^2 + |\partial_y\psi_2|^2)dy. \quad (29)$$

Through the integration, the contribution of intermolecule force and intramolecule force is obtained.

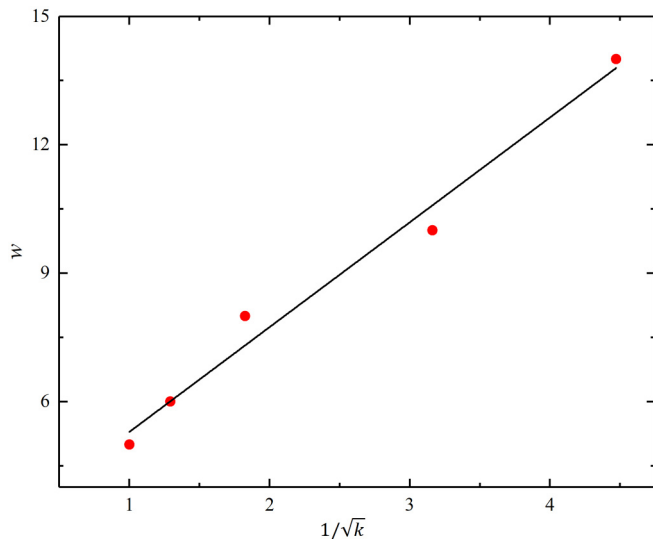


FIG. 11. Relationship between interface thickness and the scaling coefficient k of the EOS.

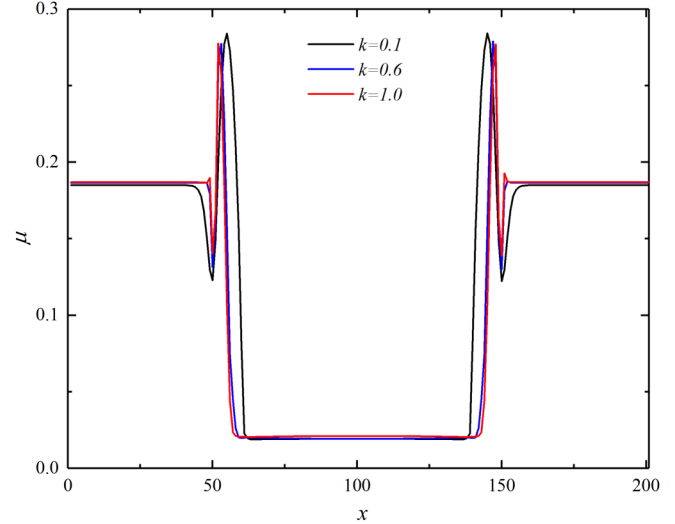


FIG. 12. Chemical potential distribution after bubble reaches the equilibrium at $y = 100$ lu with different k values.

The comparison between the surface tension obtained by theoretical analysis and that obtained by Laplace law is shown in Fig. 13(a); the numerical result agrees well with the theoretical analysis and the maximum error between theoretical analysis and numerical results is less than 2%. Figure 13(b) depicts the surface tension caused by the intermolecule and intramolecule interaction forces. As defined in Eq. (28), the surface tension caused by intermolecule force is not related to the intermolecule interaction strength $G_{\alpha,\alpha}$. However, the surface tension caused by intramolecule force depends on the intramolecule interaction strength $G_{\alpha,\bar{\alpha}}$, and decreases with the decreasing of $G_{\alpha,\bar{\alpha}}$. Through theoretical analysis, the surface tension σ_{intra} caused by the intramolecule force is only 1%–2.3% of the surface tension σ_{inter} caused by the intermolecule force in the present model.

E. Effect of viscosity ratio

To ensure the numerical stability of large-density-ratio MCMP pseudopotential models, most previous studies set the viscosity ratio to 1 and ignored this parameter of the fluid system, an oversight that may affect the evolution of the velocity field. The gas-liquid viscosity ratio may be very large in actual multiphase phenomena, e.g., the viscosity ratio between air and water is about 15, and so the influence of different viscosity ratios on the density distribution is analyzed with $k = 0.6$ and $R_0 = 50$. Firstly, the relaxation coefficient of the gas component is set to 1.0625, giving a corresponding viscosity of gas of 0.1875, while the relaxation coefficients of the liquid component are set to $\tau_l = 0.5375, 0.6125,$ and 1.0625 and the corresponding gas-liquid viscosity ratios are set to $M = 15, 5,$ and 1 . The density profile at $y = 100$ lu after the fluid system reaches equilibrium is shown in Fig. 14(a). The viscosity of the liquid phase only affects the density distribution of gas components in the liquid phase near the interface at large density ratios. The concentration of gas components in the liquid phase near the interface increases as the viscosity of the liquid component increases, but the concentration of gas components in the bubble and the

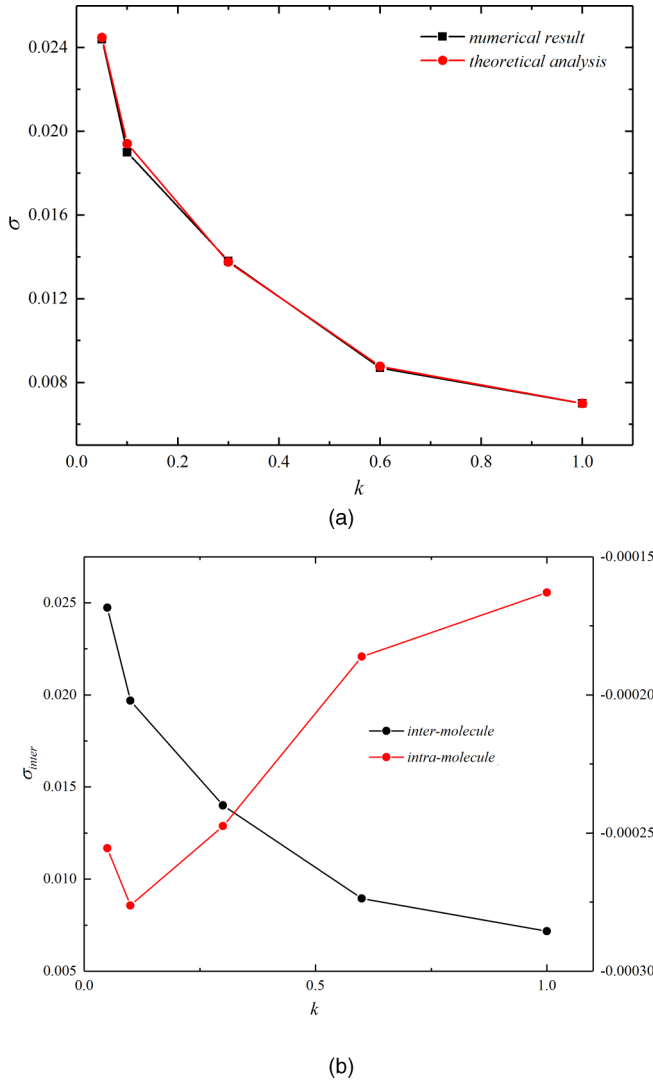


FIG. 13. (a) The comparison of the surface obtained from theoretical analysis and Laplace law. (b) The contribution of the inter-molecule and intramolecule interaction forces on surface tension.

concentration of liquid components outside the bubble are not affected by changes to the viscosity of the liquid components. Next, the relaxation coefficient of the liquid component is set to 0.5375, giving a corresponding liquid viscosity of 0.0125, while the relaxation coefficient of the gas component is set to $\tau_l = 0.5375$, 0.6875, and 1.0625 and the corresponding gas-liquid viscosity ratios are set to 1, 5, and 15. The density profile at $y = 100$ lu after the fluid system reaches equilibrium is shown in Fig. 14(b). The density profile lines at $y = 100$ lu with different gas viscosities overlap. The variation of the gas viscosity has little effect on the distribution of the density field. The results show no dependence between the density distribution and the viscosity ratio at high density ratios.

F. Bubble dissolution process under pressure

In the computational domain shown in Fig. 1, p_∞ is the pressure of the surrounding liquid and p_v is the pressure inside the bubble. The initial radius of the bubbles is set to $R_0 = 50$ lu. Considering the numerical stability and physical reality

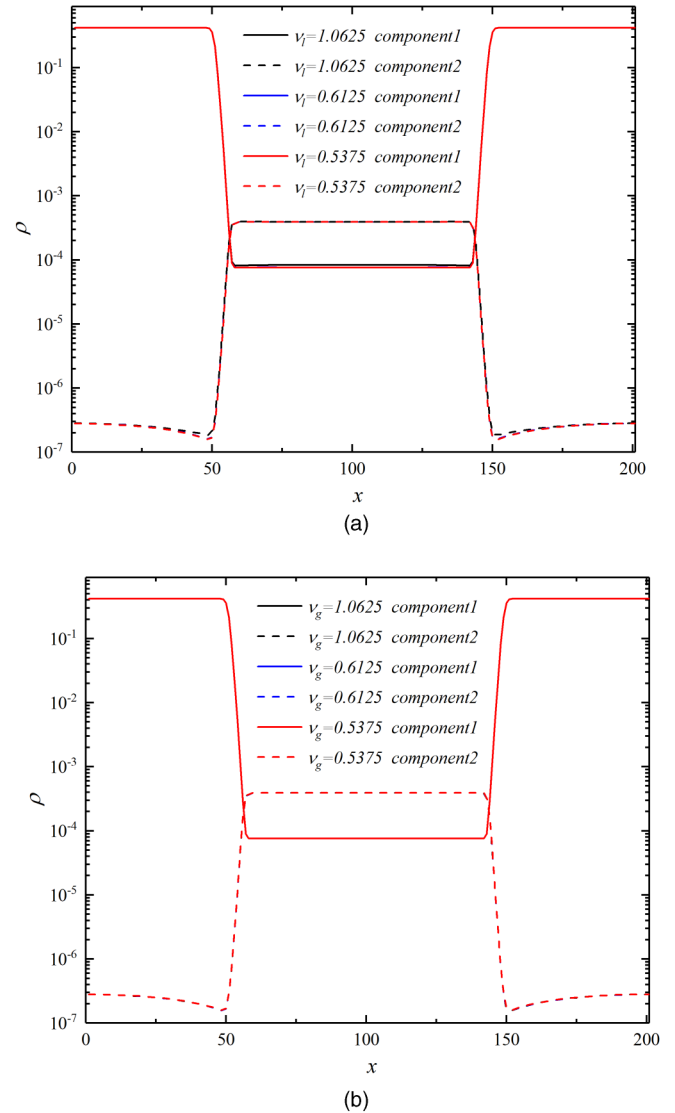


FIG. 14. Influence of different gas-liquid viscosity ratios on the gas and liquid component density distribution at $y = 100$ lu: (a) variation of liquid viscosity; (b) variation of gas viscosity.

of the simulation results, the EOS scaling coefficient k is set to 0.6. The relaxation coefficient of the gas component is chosen as $\tau_g = 1.0625$, while the relaxation coefficient of the liquid component is chosen as $\tau_l = 0.5375$ with a corresponding gas-liquid viscosity ratio of $v_g/v_l = 15$. The corresponding density field is initialized according to (24), the initial density of the liquid component in the bubble is set to $\rho_{l-in} = 0.0001$, and the initial density of the gas component is $\rho_{g-in} = 0.0003$, while the initial density of the gas component outside the bubble is $\rho_{g-in} = 0.000001$. The other parameters are the same as those in Sec. III A.

Figure 15 shows the process of bubble dissolution with $k = 0.6$ and $\Delta p = 0.01356$. When the pressure difference between the liquid and gas phases is greater than in the equilibrium state, the force balance at the bubble interface is broken. The gas density of both components increases in the bubble as its diameter decreases, and so the density field of both components changes greatly across the whole

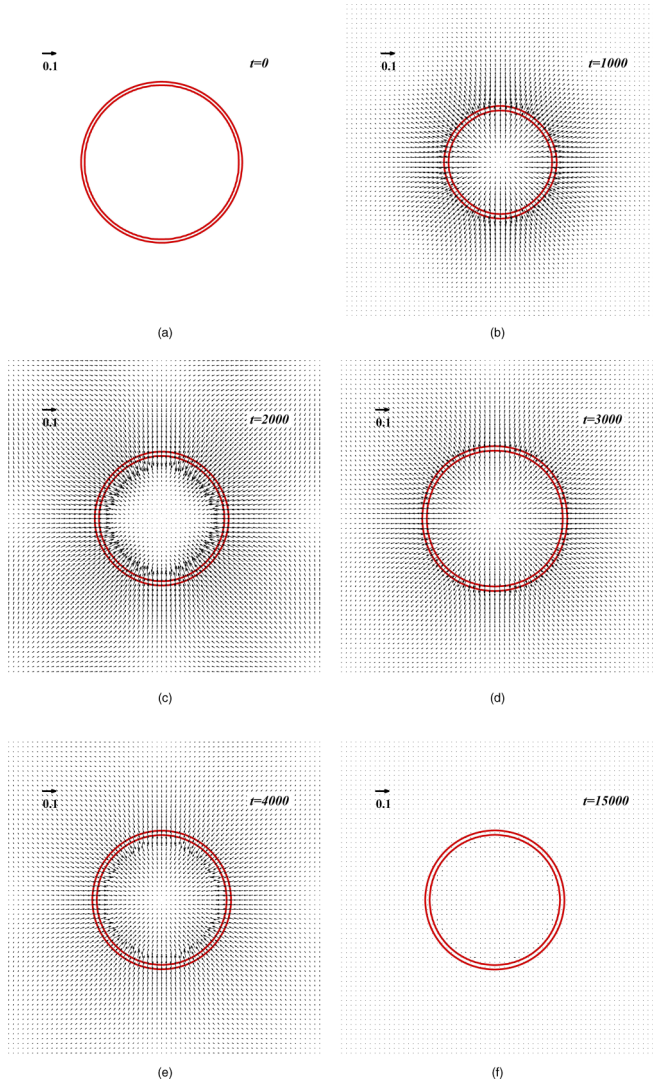


FIG. 15. Velocity distribution of fluid system during bubble dissolution process with $k = 0.6$ and $\Delta p = 0.01356 \text{ mu lu}^{-1} \text{ tu}^{-2}$ at different time steps: (a) $t = 0$, (b) $t = 1000 \text{ tu}$, (c) $t = 2000 \text{ tu}$, (d) $t = 3000 \text{ tu}$, (e) $t = 4000 \text{ tu}$, and (f) $t = 15000 \text{ tu}$.

computational domain. The bubble radius is compressed to the minimum of $R = 26 \text{ lu}$ at $t = 345 \text{ tu}$, as shown in Fig. 16, while the flow velocity on the interface is zero and the pressure inside the bubble is greater than that outside. The bubble then oscillates and its diameter increases rapidly, with the radius reaching the maximum of $R = 47 \text{ lu}$ at $t = 640 \text{ tu}$ after rebounding, as shown in Fig. 16, at which time the pressure inside the bubble is once again smaller than that outside. The pressure difference then oscillates, causing fluctuations in the bubble radius, gas phase density, and dissolution mass of the gas component. The bubble radius reaches equilibrium at $t = 15000 \text{ tu}$, as shown in Fig. 16, at which point the pressure difference inside and outside of the gas is balanced and the concentration and mass of the dissolved gas component reaches equilibrium. The maximum flow velocity occurs near the interface while the bubble is oscillating. When the bubble is compressed, the velocity is perpendicular to the interface and points toward the center of the bubble. In contrast, the

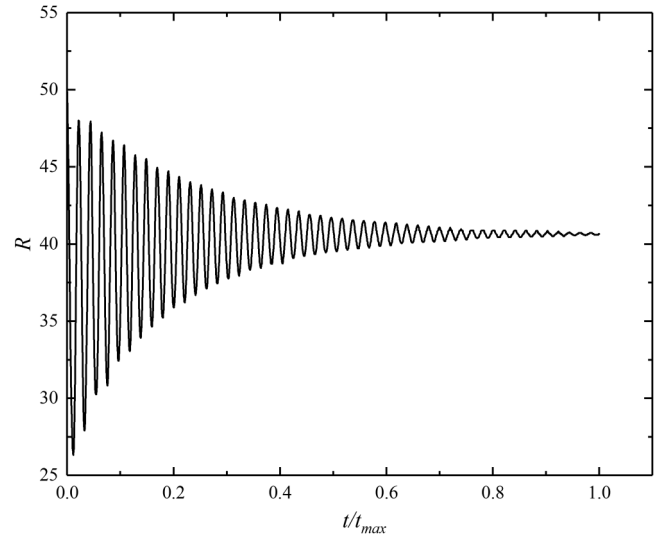


FIG. 16. Variation in the radius of the bubble with time when $k = 0.6$ and $\Delta p = 0.01356 \text{ mu lu}^{-1} \text{ tu}^{-2}$.

velocity is perpendicular to the interface and pointing outside of the bubble as the bubble rebounds. The maximum velocity when the fluid system reaches equilibrium is much smaller than that as the bubble is oscillating. The smaller spurious currents do not affect the real velocity distribution of the fluid system, demonstrating that our MCMP pseudopotential model has good numerical stability.

In the present study, the total dissolved gas mass is obtained by adding all of the dissolved gas densities in the grid nodes of the surrounding liquid:

$$M_{g\text{-out}} = \sum \rho_{g\text{-out}}(\mathbf{x}), \quad (30)$$

where $M_{g\text{-out}}$ is the total dissolved gas mass. Figure 17 presents the variation in the dissolved gas mass with $k = 0.6$ and $\Delta p = 0.01356 \text{ mu lu}^{-1} \text{ tu}^{-2}$. The dissolved gas mass increases rapidly during the first bubble compression process, then oscillates with the bubble radius. Goldman *et al.* [2]

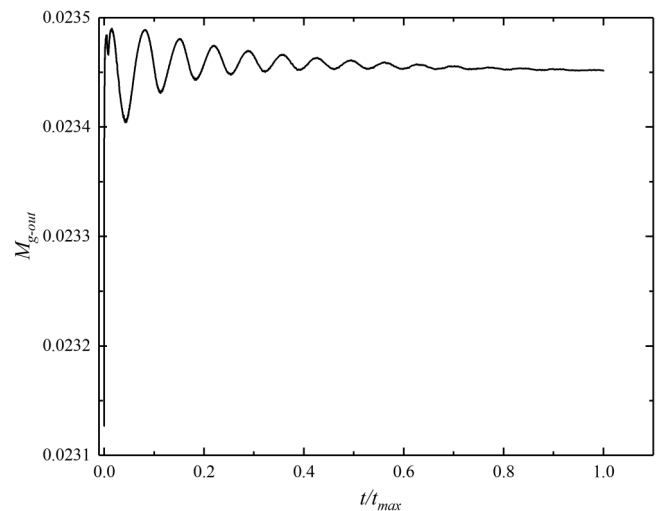


FIG. 17. Variation in dissolved gas mass with time when $k = 0.6$ and $\Delta p = 0.01356 \text{ mu lu}^{-1} \text{ tu}^{-2}$.

indicated that a stable bubble radius is achieved by mechanical equilibrium, whereas a stable concentration is achieved by chemical equilibrium; that is, the concentration gradient inside and outside the bubble reaches equilibrium. Due to the diffusion process of dissolved gas being much slower than that of bubble oscillation, the oscillation period of the dissolved gas is much longer than that of the bubble radius.

The variation in the gas component density, liquid component density, and total density at $y = 100$ lu with respect to the initial pressure difference when $k = 0.6$ is shown in Fig. 18. Figure 18(a) shows that the density of the gas component outside the bubble increases as the pressure increases, causing the dissolved gas concentration to increase as well. As the gas component is set as an ideal gas in our model, the density of the gas component inside the bubble increases linearly with any increase in pressure. The variation in the liquid component density in the fluid system with the pressure difference is shown in Fig. 18(b). The initial pressure difference has little effect on the density of the liquid component outside the bubble, but the density of the liquid component in the bubble increases as the pressure increases. Figure 18(c) shows the variation in the total density with the initial pressure difference. Although the density of the gas component in the liquid phase is greatly affected by the pressure, there is an order of magnitude difference between the density of the gas component and that of the liquid component outside the bubble. Variations in the initial pressure difference have little influence on the total density of the liquid phase. However, the density of the gas component in the bubble is similar to that of the liquid component, so the densities of both the gas component and the liquid component increase as the bubble is compressed, causing the total density in the bubble to increase.

As the density of the gas component in the liquid phase increases, the mass and concentration of dissolved gas increase. Previous studies have shown that the concentration of dissolved gas increases with pressure increases in an airtight container [6,7]. The concentration of dissolved gas is the mass concentration, which is defined as follows in the present study:

$$C = \frac{M_{g-out}}{V_l}, \tag{31}$$

where C is the mass concentration of dissolved gas and V_l is the volume of the liquid phase.

The numerical simulation results show that both the mass and concentration of dissolved gas increase linearly as the initial pressure difference increases (see Fig. 19). The mass of dissolved gas increases from 0.0094 to 0.0281 as the initial pressure difference increases from 0.001 33 to 0.017 mu lu⁻¹ tu⁻², and the dissolved gas concentration also increases from 9.15×10^{-5} to 0.0027.

It is obviously important to validate the numerical results obtained here for predicting the stability, growth, and dissolution of gas bubbles. This can be done using Henry's law. It is well known that the gas solubility in liquids and the partial pressure of the gas are proportional to the molar concentration of the gas in the solution in an airtight container at a certain temperature [3,47], that is,

$$p_g = K_{CB} \times C_B, \tag{32}$$

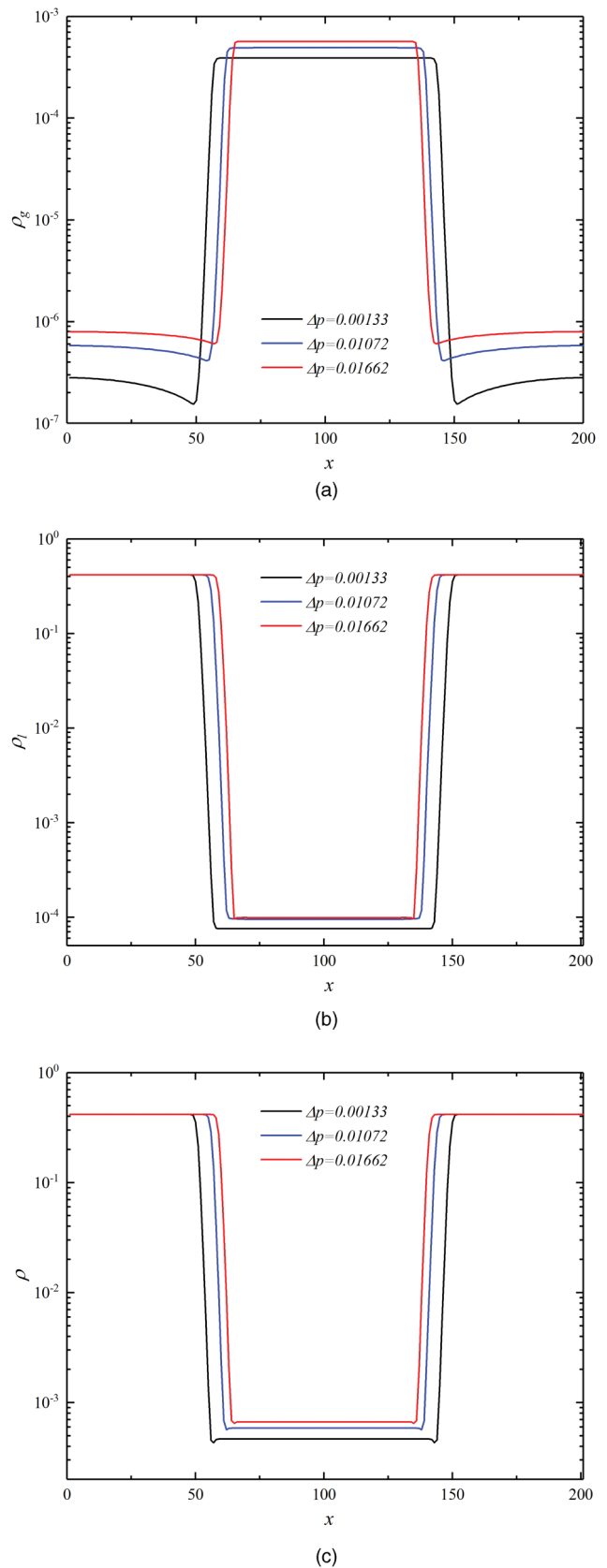


FIG. 18. Influence of initial pressure difference on gas component density, liquid component density, and total density at $y = 100$ lu ($k = 0.6$): (a) gas component density distribution, (b) liquid component density distribution, and (c) total density distribution.

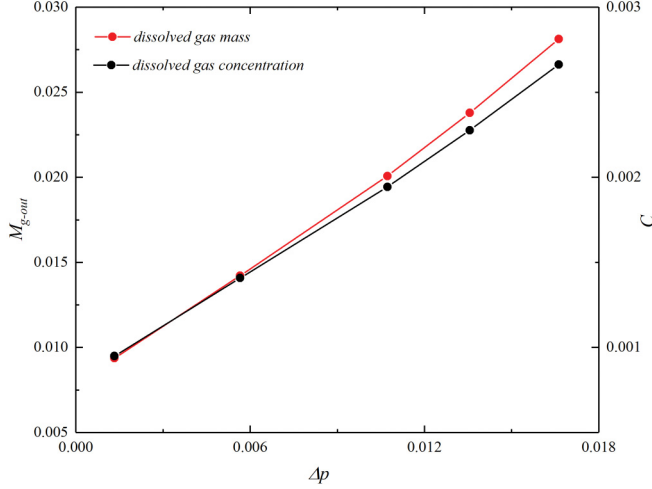


FIG. 19. Relationship between the mass and concentration of dissolved gas and the initial pressure difference with $k = 0.6$ and $\Delta p = 0.01356 \text{ mu}^{-1} \text{ tu}^{-2}$.

where p_g is the gas phase partial pressure after the system reaches the equilibrium state, K_{CB} is Henry's coefficient, and C_B is the molar concentration. The concentration of dissolved gas C defined in this study is proportional to the molar concentration C_B , with $C = C_B M_{O_g}$, where M_{O_g} is the number of moles. Thus, there is a linear relationship between the gas phase partial pressure p_v and the concentration of dissolved gas C :

$$p_g = K_C C. \quad (33)$$

Earlier research stated that all gaseous solutes will obey Henry's law to an excellent approximation. The numerical results show that the concentration of dissolved gas is proportional to the gas partial pressure, as shown in Fig. 20, and the linear fitting coefficient K_C is approximately 36.44. The results indicate that the numerical method can predict the time

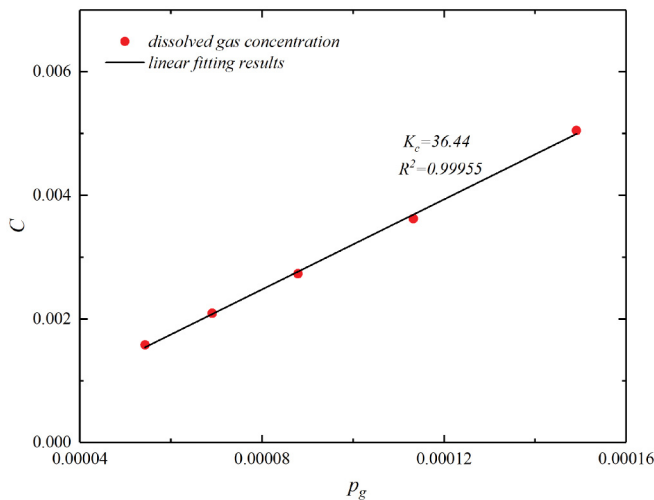


FIG. 20. Relationship between the dissolved gas concentration and partial pressure of component 1 in the surrounding liquid after the fluid system reaches equilibrium.

evolution of bubble growth and the concentration of a single ideal bubble.

The choice of parameters has only been considered from the perspective of numerical stability, and the conversion between lattice units and real physical units has not been considered in the present study. Additionally, the factors influencing the gas dissolution process have not been fully considered, including the diffusion rate and surface tension. The above-mentioned limitations to this study will be overcome in future work.

IV. CONCLUSIONS

In this paper, we have proposed a multicomponent multiphase pseudopotential lattice Boltzmann model that is suitable for high density ratios and high viscosity ratios. The proposed formulation uses the MRT collision operator, EDM force scheme, and scaling coefficient of the EOS. Laplace's law was used to validate the LBM, which was then used to simulate the dissolution process of bubbles under different pressures with a liquid-gas density ratio of 1050 and a viscosity ratio of 15. The variation of dissolved gas mass, gas phase density, and dissolved gas concentration after the fluid system reached equilibrium was analyzed under different initial pressure differences.

Adjusting the scaling coefficient k of the EOS changes the surface tension and interface thickness, and affects the gas and liquid density distributions after the fluid has reached equilibrium. The surface tension increases with k , while spurious currents decrease with smaller values of k . Furthermore, it has been proved that the gas-liquid interface thickness w is proportional to $1/\sqrt{k}$. Considering the influence of k on the surface tension, interface thickness, and gas-liquid density ratio after the fluid system has reached equilibrium, it is suggested that k should be set between 0.6 and 1. Furthermore, the effect of the kinematic ratio has also been investigated, with the results showing no dependence between the density distribution and viscosity ratio at high density ratios.

The dissolution process of a single bubble under pressure was successfully simulated. The mass and concentration of the dissolved gas were observed to oscillate with the bubble radius, and the equilibrium mass and concentration of dissolved gas increased linearly with the initial pressure difference. The initial pressure difference mainly affects the density distribution of the gas phase and has little effect on the density distribution of the liquid phase. Once the fluid system has reached equilibrium, the concentration of dissolved gas is proportional to the partial pressure of the gas phase, which satisfies Henry's law.

In summary, the MRT collision operator, EDM external force scheme, and scaling coefficient k were applied to improve the numerical stability of the MCMP pseudopotential model at high density ratios and various viscosity ratios. However, the model does not always achieve thermodynamic consistency. As presented in our study, both the EDM external force term and the k method lead to the thermodynamic inconsistency. Therefore, the external force term of Li *et al.* [35] is introduced to overcome this limitation in our follow-up study, and from the preliminary study, we found the

model with the external force scheme of Li *et al.* [35] can achieve thermodynamic consistency and low spurious currents without using the k method. The influence of several factors, including the diffusivity parameter, pressure difference, on the real bubble dissolution process will also be considered.

ACKNOWLEDGMENTS

This work was supported by the National Science Fund for Distinguished Young Scholars (Grant No. 51625901) and the National Natural Science Foundation of China (Grant No. 51879176).

X.H. and J.Z. contributed equally to this work.

-
- [1] H. Sun, J. Yao, S. H. Gao, D. Y. Fan, C. C. Wang, and Z. X. Sun, Numerical study of CO₂ enhanced natural gas recovery and sequestration in shale gas reservoirs, *Int. J. Greenhouse Gas Control* **19**, 406 (2013).
- [2] S. Goldman, J. M. Solano-Altamirano, and K. M. Ledez, Driving force of gas-bubble growth and dissolution, *Gas Bubble Dyn. Hum. Body* **2018**, 49 (2018).
- [3] J. J. Zhou, A. Vacca, and B. Manhartgruber, A novel approach for the prediction of dynamic features of air release and absorption in hydraulic oils, *J. Fluids Eng.* **135**, 091305 (2013).
- [4] D. Geldert, J. Gulliver, and S. Wilhelms, Modeling dissolved gas supersaturation below spillway plunge pools, *J. Hydraul. Eng.* **124**, 513 (1998).
- [5] X. G. Liang, H. Tan, Z. L. Fu, and S. Y. Chou, Air bubble formation and dissolution in dispensing nanoimprint lithography, *Nanotechnology* **18**, 025303 (2007).
- [6] P. Penas-López, M. A. Parrales, D. van der Meer, D. Lohse, and J. Rodríguez-Rodríguez *et al.* The history effect in bubble growth and dissolution. Part I. Theory, *J. Fluid Mech.* **820**, 479 (2017).
- [7] J. Kwan and M. Borden, Microbubble dissolution in a multigas environment, *Langmuir* **26**, 6542 (2010).
- [8] G. Kapodistrias and P. H. Dahl, Scattering measurements from a dissolving bubble, *J. Acoust. Soc. Am.* **131**, 4243 (2012).
- [9] I. M. Krieger, G. W. Mulholland, and C. S. Dickey, Diffusion coefficients for gases in liquids from the rates of solution of small gas bubbles, *J. Phys. Chem.* **71**, 1123 (1967).
- [10] L. Liebermann, Air bubbles in water, *J. Appl. Phys.* **28**, 205 (1957).
- [11] E. Goncalves, M. Champagnac, and R. Patella, Comparison of numerical solvers for cavitating flows, *Int. J. Comput. Fluid Dyn.* **24**, 201 (2010).
- [12] E. Ghahramani, M. Arabnejad, and R. Bensow, A comparative study between numerical methods in simulation of cavitating bubbles, *Int. J. Multiphase Flow* **111**, 339 (2019).
- [13] G. Chahine, A. Kapahi, J. K. Choi, and C. S. Hsiao, Modeling of surface cleaning by cavitation bubble dynamics and collapse, *Ultrason. Sonochem.* **29**, 528 (2016).
- [14] C. T. Hsiao, J. S. Ma, and G. Chahine, Multiscale tow-phase flow modeling of sheet and cloud cavitation, *Int. J. Multiphase Flow* **90**, 102 (2017).
- [15] X. W. Shan and H. D. Chen, Lattice Boltzmann model for simulating flows with multiple phases and components, *Phys. Rev. E* **47**, 1815 (1993).
- [16] X. W. Shan and H. D. Chen, Simulation of nonideal gases and liquid-gas phase transitions by the lattice Boltzmann equation, *Phys. Rev. E* **49**, 2941 (1994).
- [17] A. K. Gunstensen, D. H. Rothman, S. Zaleski, and G. Zanetti, Lattice Boltzmann model of immiscible fluids, *Phys. Rev. A* **43**, 4320 (1991).
- [18] M. Latva-Kokko and D. Rothman, Diffusion properties of gradient-based lattice Boltzmann models of immiscible fluids, *Phys. Rev. E* **71**, 056702 (2005).
- [19] M. Swift, W. Osborn, and J. Yeomans, Lattice Boltzmann Simulation of Nonideal Fluids, *Phys. Rev. Lett.* **75**, 830 (1995).
- [20] M. R. Swift, E. Orlandini, W. R. Osborn, and J. M. Yeomans, Lattice Boltzmann simulations of liquid-gas and binary fluid systems, *Phys. Rev. E* **54**, 5041 (1996).
- [21] X. Y. He, S. Y. Chen, and R. Y. Zhang, A lattice Boltzmann scheme for incompressible multiphase flow and its application in simulation of Rayleigh–Taylor instability, *J. Comput. Phys.* **152**, 642 (1999).
- [22] Q. Li, K. H. Luo, Q. J. Kang, Y. L. He, Q. Chen, and Q. Liu, Lattice Boltzmann methods for multiphase flow and phase-change heat transfer, *Prog. Energy Combust. Sci.* **52**, 62 (2016).
- [23] X. W. Shan and G. Doolen, Multicomponent lattice-Boltzmann model with interparticle interaction, *J. Stat. Phys.* **81**, 379 (1995).
- [24] J. Bao and L. Schaefer, Lattice Boltzmann equation model for multi-component multi-phase flow with high density ratios, *Appl. Math. Modell.* **37**, 1860 (2013).
- [25] C. Stiles and Y. Q. Xue, High density ratio lattice Boltzmann method simulations of multicomponent multiphase transport of H₂O in air, *Comput. Fluids* **131**, 81 (2016).
- [26] L. Chen, Q. J. Kang, Q. Tang, B. A. Robinson, Y. L. He, and W. Q. Tao, Pore-scale simulation of multicomponent multiphase reactive transport with dissolution and precipitation, *Int. J. Heat Mass Transfer* **85**, 935 (2015).
- [27] C. Y. Zhang, P. Cheng, and W. Minkowycz, Lattice Boltzmann simulation of forced condensation flow on a horizontal cold surface in the presence of a non-condensable gas, *Int. J. Heat Mass Transfer* **115**, 500 (2017).
- [28] H. Deng, K. Jiao, Y. Z. Hou, J. W. Park, and Q. Du, A lattice Boltzmann model for multi-component two-phase gas-liquid flow with realistic fluid properties, *Int. J. Heat Mass Transfer* **128**, 536 (2019).
- [29] W. B. Zhu, M. Wang, and H. Chen, Study on multicomponent pseudo-potential model with large density ratio and heat transfer, *Int. Commun. Heat Mass Transfer* **87**, 183 (2017).
- [30] L. Chen, M. Y. Wang, Q. J. Kang, and W. Q. Tao, Pore scale study of multiphase multicomponent reactive transport during CO₂ dissolution trapping, *Adv. Water Resour.* **116**, 208 (2018).
- [31] Q. Y. Zhang, D. K. Sun, and M. F. Zhu, A multicomponent multiphase lattice Boltzmann model with large liquid–gas density ratios for simulations of wetting phenomena, *Chin. Phys. B* **26**, 084701 (2017).
- [32] A. Kupershtokh, Criterion of numerical instability of liquid state in LBE simulations, *Comput. Math. Appl.* **59**, 2236 (2010).

- [33] A. J. Hu, L. J. Li, S. X. Chen, Q. Liao, and J. B. Zeng, On equations of state in pseudo-potential multiphase lattice Boltzmann model with large density ratio, *Int. J. Heat Mass Transfer* **67**, 159 (2013).
- [34] P. Lallemand and L. S. Luo, Theory of the lattice Boltzmann method: Dispersion, dissipation, isotropy, Galilean invariance, and stability, *Phys. Rev. E* **61**, 6546 (2000).
- [35] Q. Li, K. H. Luo, and X. J. Li, Lattice Boltzmann modeling of multiphase flows at large density ratio with an improved pseudopotential model, *Phys. Rev. E* **87**, 053301 (2013).
- [36] H. Otomo, B. Crouse, and M. Dressler, D. M. Freed, I. Staroselsky, R. Y. Zhang, and H. D. Chen, Multi-component lattice Boltzmann models for accurate simulation of flows with wide viscosity variation, *Comput. Fluids* **172**, 674 (2018).
- [37] Z. Yu and L. Fan, Multi-relaxation-time interaction-potential-based lattice Boltzmann model for two-phase flow, *Phys. Rev. E* **82**, 046708 (2010).
- [38] A. Kupershtokh, D. Medvedev, and D. Karpov, On equations of state in a lattice Boltzmann method, *Comput. Math. Appl.* **58**, 965 (2009).
- [39] Z. Yu, A novel lattice Boltzmann method for direct numerical simulation of multiphase flows, The Ohio State University, 2009.
- [40] X. W. Shan, Pressure tensor calculation in a class of nonideal gas lattice Boltzmann models, *Phys. Rev. E* **77**, 066702 (2008).
- [41] P. Yuan and L. Schaefer, Equations of state in a lattice Boltzmann model, *Phys. Fluids* **18**, 042101 (2006).
- [42] T. Lee and C. Lin, A stable discretization of the lattice Boltzmann equation for simulation of incompressible two-phase flows at high density ratio, *J. Comput. Phys.* **206**, 16 (2005).
- [43] H. Zheng, C. Shu, and Y. Chew, A lattice Boltzmann model for multiphase flows with large density ratio, *J. Comput. Phys.* **218**, 353 (2006).
- [44] D. Jamet, D. Torres, and J. U. Brackbill, On the theory and computation of surface tension: The elimination of parasitic currents through energy conservation in the second-gradient method, *J. Comput. Phys.* **182**, 262 (2002).
- [45] B. Wen, X. Zhou, B. He, C. Zhang, and H. Fang, Chemical-potential-based lattice Boltzmann method for nonideal fluids, *Phys. Rev. E* **95**, 063305 (2017).
- [46] R. Benzi, L. Biferale, M. Sbragaglia, S. Succi, and F. Toschi, Mesoscopic modeling of a two-phase flow in the presence of boundaries: The contact angle, *Phys. Rev. E* **74**, 021509 (2006).
- [47] O. R. Enríquez, C. Hummelink, and G.-W. Bruggert, Growing bubbles in a slightly supersaturated liquid solution, *Rev. Sci. Instrum.* **84**, 065111 (2013).